

# UC Davis

## UC Davis Previously Published Works

### Title

Local strain inhomogeneities during electrical triggering of a metal-insulator transition revealed by X-ray microscopy.

### Permalink

<https://escholarship.org/uc/item/49b2z8t9>

### Journal

Proceedings of the National Academy of Sciences, 121(34)

### Authors

Salev, Pavel

Kisiel, Elliot

Sasaki, Dayne

et al.

### Publication Date

2024-08-20










### DOI

10.1073/pnas.2317944121

Peer reviewed



# Local strain inhomogeneities during electrical triggering of a metal–insulator transition revealed by X-ray microscopy

Pavel Salev<sup>a,1</sup> , Elliot Kiesel<sup>b,c</sup> , Dayne Sasaki<sup>d</sup> , Brandon Gunn<sup>b</sup>, Wei He<sup>b</sup>, Mingzhen Feng<sup>d</sup>, Junjie Li<sup>b</sup> , Nobumichi Tamura<sup>e</sup> , Ishwor Poudyal<sup>f</sup>, Zahirul Islam<sup>c</sup> , Yayoi Takamura<sup>d</sup> , Alex Frano<sup>b</sup> , and Ivan K. Schuller<sup>b</sup> 

Affiliations are included on p. 7.

Edited by Laura Greene, Florida State University, Tallahassee, FL; received October 15, 2023; accepted July 5, 2024

Electrical triggering of a metal–insulator transition (MIT) often results in the formation of characteristic spatial patterns such as a metallic filament percolating through an insulating matrix or an insulating barrier splitting a conducting matrix. When MIT triggering is driven by electrothermal effects, the temperature of the filament or barrier can be substantially higher than the rest of the material. Using X-ray microdiffraction and dark-field X-ray microscopy, we show that electrothermal MIT triggering leads to the development of an inhomogeneous strain profile across the switching device, even when the material does not undergo a pronounced, discontinuous structural transition coinciding with the MIT. Diffraction measurements further reveal evidence of unique features associated with MIT triggering including lattice distortions, tilting, and twinning, which indicate structural nonuniformity of both low- and high-resistance regions inside the switching device. Such lattice deformations do not occur under equilibrium, zero-voltage conditions, highlighting the qualitative difference between states achieved through increasing temperature and applying voltage in nonlinear electrothermal materials. Electrically induced strain, lattice distortions, and twinning could have important contributions in the MIT triggering process and drive the material into nonequilibrium states, providing an unconventional pathway to explore the phase space in strongly correlated electronic systems.

metal–insulator transition | resistive switching | X-ray microdiffraction | dark-field X-ray microscopy | in operando microscopy

Applying voltage to metal–insulator transition (MIT) materials can trigger a large resistance change producing volatile resistive switching (1, 2). MIT switches are actively pursued for practical applications, such as selectors in crossbar memory arrays (3, 4), rf and optical switches (5–7), and spiking devices for neuromorphic and stochastic computing (8–13). Physical mechanisms that drive electrical MIT triggering remain a subject of debate. Under an electric stimulus, both Joule heating and electrostatic charge doping can contribute to MIT triggering (14, 15). Because of the intricate coupling between charge, spin, lattice, and orbital degrees of freedom in MIT materials (16–21), experimental studies providing diverse information about the electrically induced changes in the electronic, magnetic, and structural order are necessary to establish the basic understanding of the MIT triggering process.

Some MIT materials, such as  $\text{VO}_2$  and  $\text{V}_2\text{O}_3$ , have a pronounced 1st-order structural transition coinciding with the electronic transition (22). Transmission electron microscopy and micro- and nanodiffraction measurements in  $\text{VO}_2$  switching devices have shown that when an electric stimulus triggers the MIT, the corresponding structural transition is also induced, which results in the formation of a rutile metal filament inside a monoclinic insulator matrix (23–25). Other materials, for example,  $\text{V}_3\text{O}_5$ ,  $\text{NbO}_2$ ,  $\text{SmNiO}_3$ , and  $\text{La}_{0.7}\text{Sr}_{0.3}\text{MnO}_3$  (LSMO), do not undergo a pronounced, discontinuous structural transition coinciding with the MIT under equilibrium conditions. Such materials may exhibit only subtle structural changes across the phase transition, e.g., bond disproportioning or Jahn–Teller distortions (26, 27). Crystal structure evolution under strong electric stimuli remains unknown in MIT switching materials that do not have pronounced, discontinuous structural transitions. Because the MIT can be triggered at temperatures hundreds of Kelvins below the transition temperature ( $T_c$ ) (28–30), it can be expected that thermal gradients associated with the electrically induced local phase transition may induce a substantial thermal expansion of the crystal lattice, altering the local strain. It is well established that MIT materials are highly susceptible to crystal lattice deformations (31–34); therefore, the development of local strain during the electrical switching may play an important role in the MIT triggering process.

## Significance

Electrically actuated phase-change materials are actively explored as candidates for improving the scalability and energy efficiency of conventional, neuromorphic, and reservoir computing electronics. While the significance of structure–function relationships is universally acknowledged, studies of electrically driven structural evolution in phase-change materials are highly challenging because they require performing local, in operando measurements. Here, we explore structural signatures of electrically triggered metal–insulator phase transition using X-ray diffraction microscopy. We demonstrate that the application of strong electric stimuli creates local inhomogeneous strain and distorts the crystal lattice symmetry, yielding a structural state that differs qualitatively from thermal equilibrium. Harnessing these voltage-induced structural changes may provide unique pathways for enabling novel device architectures and exploring nonequilibrium material phases.

Author contributions: P.S., E.K., N.T., Z.I., Y.T., A.F., and I.K.S. designed research; P.S., E.K., D.S., B.G., W.H., M.F., J.L., N.T., I.P., and Z.I. performed research; P.S., E.K., and D.S. analyzed data; and P.S., E.K., B.G., and Y.T. wrote the paper.

The authors declare no competing interest.

This article is a PNAS Direct Submission.

Copyright © 2024 the Author(s). Published by PNAS. This open access article is distributed under [Creative Commons Attribution License 4.0 \(CC BY\)](https://creativecommons.org/licenses/by/4.0/).

<sup>1</sup>To whom correspondence may be addressed. Email: pavel.salev@du.edu.

This article contains supporting information online at <https://www.pnas.org/lookup/suppl/doi:10.1073/pnas.2317944121/-/DCSupplemental>.

Published August 15, 2024.

In this work, we explored the electrically driven crystal structure evolution in LSMO switching devices with the La:Sr ratio of 0.7:0.3 as a representative material that does not have a 1st-order structural transition coinciding with the MIT. LSMO is a particularly interesting system because it exhibits a metal-to-insulator switching (35–37), in contrast to the more common insulator-to-metal switching observed in materials such as  $\text{VO}_2$ ,  $\text{V}_2\text{O}_3$ ,  $\text{V}_3\text{O}_5$ ,  $\text{NbO}_2$ ,  $\text{SmNiO}_3$ , etc. MIT triggering in LSMO also drives unusual magnetic phenomena, including the development of uniaxial magnetic anisotropy (36) and anomalous magnetotransport properties (37), whose physical origins are not yet fully understood. Here, we employed a combination of conventional X-ray microdiffraction and recently developed dark-field X-ray microscopy (DFXM) techniques to explore the structural signatures of electrical MIT triggering. We observed that driving LSMO across the MIT results in the strain development, even though LSMO does not have a discontinuous structural transition coinciding with the MIT. The measured strain displayed a spatial profile consistent with the locally induced MIT switching inside the device. In contrast to the previous magneto-optical phase mapping experiments (35), X-ray microscopy revealed that electrical MIT triggering is an extremely complex process from the structural perspective and its representation as the coexistence of local high- and low-resistance regions is highly oversimplified. X-ray microscopy showed that the crystal lattice in the regions that locally undergo switching into the high-resistance state experiences twinning and structural distortions. Strain also propagates throughout the device causing lattice tilting in the regions that do not undergo switching. The structural response observed in the entire device area directly reveals the nonlocal effect of electrical MIT triggering, which remained hidden in the previous phase mapping experiments. Our results show that lattice evolution in the switching devices under applied voltage qualitatively differs from equilibrium thermal behavior, indicating that electrically induced structural changes can be significant even in materials that do not undergo a pronounced structural transition coincident with the MIT.

## Results

**X-ray Microdiffraction.** We explored the strain development during electrical MIT triggering in two-terminal  $\text{La}_{0.7}\text{Sr}_{0.3}\text{MnO}_3$  devices (Fig. 1A). The devices were patterned in a 50-nm-thick film epitaxially grown on a  $\text{SrTiO}_3$  (STO) substrate (38, 39). LSMO transitions from a low-resistance ferromagnetic metal to high-resistance paramagnetic bad metal at  $T_c \sim 340$  K (40). While both low- and high-temperature phases are nominally metals, the phase transition in LSMO is commonly referred to as an MIT to highlight the large resistance contrast between the low- and high-temperature phases. Applying voltage to LSMO can trigger the MIT, even at the temperatures that are hundreds of Kelvins below  $T_c$  (35). This electrical MIT triggering is mediated by Joule heating, and it produces volatile resistive switching, i.e., a switching that persists while the voltage is applied but automatically resets when the voltage is turned off. The switching occurs in a characteristic spatial pattern: the formation of a high-resistance barrier in a direction perpendicular to the current flow (35–37), in contrast to the more commonly observed filamentary percolation (41–43). Even though the MIT in LSMO does not involve pronounced structural changes (see, for example, the temperature-dependent X-ray diffraction in an LSMO film in *SI Appendix, Fig. S1*), thermal gradients associated with the Joule-heating-driven barrier formation can

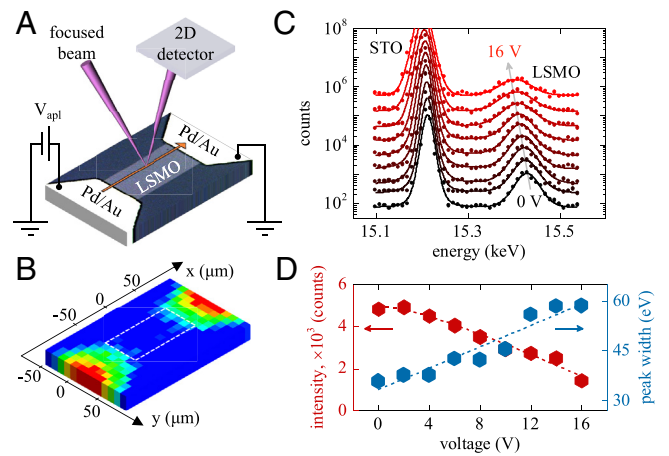


**Fig. 1.** (A) Schematic of the X-ray microdiffraction measurement setup. A focused X-ray beam acquires local diffraction patterns at several locations across the LSMO device length. The device is held under a constant applied voltage. The device picture is an optical microscopy image. (B) X-ray fluorescence map of the LSMO device. The bright regions correspond to the Pd/Au electrodes. The dashed white rectangle indicates the LSMO device location. (C) Local diffraction patterns acquired at the center of LSMO device under applied voltages in the 0 to 16 V range at 2 V step. The diffraction patterns were recorded in the vicinity of the (007) STO Bragg peak. The shift of the LSMO peak toward lower energies with increasing voltage indicates the lattice expansion. The curves are vertically offset for clarity. (D) Voltage dependence of the integrated intensity (red symbols) and FWHM (blue symbols) of the LSMO (007)<sub>pc</sub> Bragg peak. The lines are guides to the eye. All measurements were performed at 180 K.

be expected to generate a substantial strain within the device, which we investigate in this work.

We employed X-ray microdiffraction to directly probe the local lattice expansion in the LSMO devices during electrical MIT triggering (Fig. 1A). These measurements were performed at the beamline 12.3.2 of the Advanced Light Source at Lawrence Berkeley National Laboratory. The X-ray beam was focused to a  $\sim 5$   $\mu\text{m}$  spot using Kirkpatrick–Baez mirrors. Diffraction patterns were acquired at multiple locations along the device length while holding the device under constant voltages in the 0 to 16 V range. The focused beam was kept fixed at a  $45^\circ$  angle relative to the sample surface, and the diffraction data were acquired by scanning the beam energy through a 15.3 to 16 keV range, which corresponded to the vicinity of the (007) Bragg peak of the STO substrate. The measurements near this higher-order Bragg peak helped minimizing the overlap between the STO and LSMO Bragg peaks. The diffracted beam was collected by a 2D detector. The device size was  $50 \times 100$   $\mu\text{m}^2$ . Individual switching devices were located using X-ray fluorescence scans by observing the fluorescence from the Pd/Au electrodes within a 9 to 10 keV range (Fig. 1B). All X-ray microdiffraction measurements were performed at a base temperature of 180 K.

We observed that an applied voltage induces a significant out-of-plane lattice expansion in the LSMO device. Fig. 1C shows the diffraction patterns acquired locally at approximately the center of the device while applying voltages in the 0 to 16 V range in 2 V steps. As the voltage increases, the LSMO Bragg peak progressively shifts toward lower energies, indicating an increase of the lattice  $d$ -spacing. Because the LSMO device experiences substantial Joule heating (the maximum dissipated power reached  $\sim 300$  mW in our experiments), the Bragg peak shift under an applied voltage can be attributed to thermal lattice expansion. We found, however, that there are qualitative differences between the voltage/Joule heating-induced lattice expansion seen here as compared to equilibrium thermal properties. Under an applied voltage,

the integrated Bragg peak intensity decreases rapidly, by a factor of  $\sim 3.5$  at 16 V (Fig. 1D, red line). Simultaneously, the Bragg peak width increases by a factor of  $\sim 2$  at 16 V (Fig. 1D, blue line). Because Joule heating is expected to substantially increase the device temperature, one might expect that the Debye-Waller factor may account for the peak intensity reduction. However, LSMO Bragg peak intensity and width have a weak temperature dependence under equilibrium, zero-voltage conditions (SI Appendix, Fig. S1). The peak intensity decreases by  $\sim 6\%$  and the peak width increases by only 0.4% between 180 K and 400 K at zero voltage. We conclude, therefore, that the Debye-Waller factor does not have a significant contribution in our experiments. Under the applied voltage, the observed  $\sim 2\times$  increase of the peak width may indicate a spatially inhomogeneous lattice expansion (lateral, i.e., across the device area, and/or vertical, i.e., across the film thickness) at the length scales below the experimental resolution ( $\sim 5\ \mu\text{m}$ ). Because the peak width increase was also accompanied by the  $\sim 3.5\times$  decrease of the integrated peak intensity, it is unlikely that such an inhomogeneous lattice expansion is due only to the formation of local regions with different strain. The decrease of the integrated intensity may be due to a change of the lattice form factor, suggesting that the voltage-induced heating may lead to asymmetric in-plane vs. out-of-plane lattice expansion and/or to lattice distortions, thereby reducing the X-ray scattering efficiency. The observation of this inhomogeneous lattice deformation suggests that electrical MIT triggering produces a state that is structurally distinct from the equilibrium high-temperature phase at zero voltage, a feature that has not been observed in the previous phase mapping experiments (35).

After observing voltage-induced lattice expansion in the LSMO device center, we next investigate the expansion in different parts of the device. Fig. 2A shows the out-of-plane strain measured at multiple locations across the device length in  $10\ \mu\text{m}$  steps while applying constant voltages in the 0 to 16 V range in 2 V steps. The strain is defined with respect to the out-of-plane  $d$ -spacing measured at 0 V. Below 8 V, the lattice expansion is the same throughout the device, which is likely due to the uniform Joule heating that precedes the electrothermal MIT triggering (35).

Above 8 V, however, the induced strain is larger in the center region (0.14% at 16 V) than at the device edges (0.09% at 16 V), resulting in bell-shaped strain profiles. This inhomogeneous lattice expansion at higher voltages is consistent with the previous magneto-optical and electrical observations of the high-resistance paramagnetic barrier formation inside the ferromagnetic metal matrix in LSMO devices during MIT triggering (35–37). Because the barrier's resistance is much higher than the metallic matrix resistance, the barrier focuses the dissipated power and experiences strong Joule heating. Larger local Joule heating leads to larger local lattice thermal expansion, as we have observed in the X-ray microdiffraction experiments.

Analysis of the LSMO Bragg peak width and intensity profiles across the device length further shows that the voltage-driven lattice evolution differs in the device center compared to the device edges, supporting the picture that Joule heating is focused inside the switched high-resistance barrier. At zero voltage, both the peak intensity and width have only small variations with no discernible trend across the device length (dark gray points in Fig. 2B and C). At 16 V, the intensity and width profiles form bell-shaped curves (red points in Fig. 2B and C) with the maximum near the device center, identical to the strain maximum location in the lattice expansion profile plot (Fig. 2A). The lower peak intensity and broader peak width at the device center at 16 V suggest that the larger local lattice expansion is accompanied by lattice symmetry distortions, likely due to the strain accommodation, as discussed later in the paper. Importantly, X-ray microscopy shows that the unswitched regions outside of the high-resistance barrier, i.e., regions where LSMO remains in the metallic phase, are also affected by local MIT triggering. These regions develop strain and have reduced intensity and increased width of the Bragg peak. Therefore, metallic regions in the switched device are structurally distinct from the equilibrium low-temperature state at zero voltage.

The development of strain inhomogeneities across the device length correlates well with the  $I$ - $V$  characteristics of the LSMO device. The  $I$ - $V$  curve (Fig. 2D) has two distinct features. The first feature is the onset of negative differential resistance (NDR) at  $\sim 8$  V, i.e., a part of the curve where the  $dV/dI$  slope is negative.

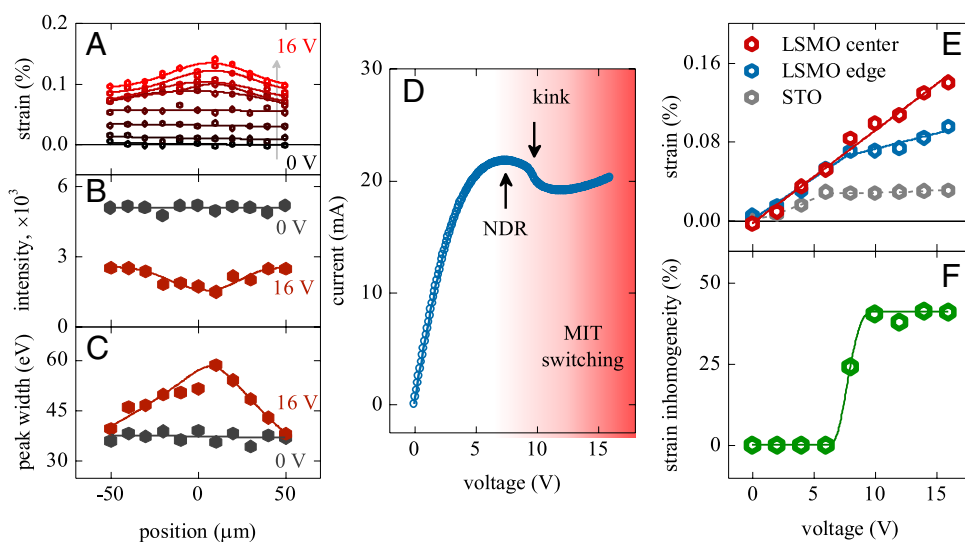


**Fig. 2.** (A) Strain profiles across the LSMO device length measured under an applied voltage in the 0 to 16 V range in 2 V steps. The development of bell-shaped profiles above 8 V, indicating that larger lattice expansion at the device center, can be observed. (B and C) Integrated intensity (B) and width (C) of the LSMO (007)<sub>pc</sub> Bragg peak measured at several locations across the device length while in equilibrium (0 V, dark gray symbols) and above the MIT triggering threshold (16 V, red symbols). The lines are guides to the eye. (D)  $I$ - $V$  curve of the LSMO device exhibiting NDR and a kink at the MIT triggering threshold voltage. (E) Strain in LSMO at the center (red symbols) and edge (blue symbols) of the device as a function of applied voltage. Gray symbols show strain in the STO substrate averaged over the device length. The lines are guides to the eye. (F) Strain inhomogeneity that develops in LSMO as a function of applied voltage. The strain inhomogeneity rapidly increases at the NDR onset voltage and reaches a stable value at the MIT triggering threshold. All measurements were performed at 180 K.

Previously, it was found that the NDR onset precedes MIT triggering and corresponds to the development of a moderate voltage distribution inhomogeneity across the device length (35). The second important feature in the  $I$ - $V$  curve is the kink at  $\sim 10$  V. At this kink, the current decreases quickly with increasing voltage, indicating a rapid increase of the device resistance. In the previous magneto-optical measurements, this kink corresponded to local phase-transition triggering in LSMO and the formation of a paramagnetic barrier inside the device (35). In the present microdiffraction experiments, we observed that the lattice expansion is the same across the device length (Fig. 2E) up to the NDR onset in the  $I$ - $V$  curve ( $\sim 8$  V, Fig. 2D). In the NDR region, the voltage dependence of the strain in the device center (red symbols in Fig. 2E) continues to follow approximately the same trend as before the NDR onset. The lattice expansion at the edges, however, slows down (blue symbols in Fig. 2E). The initial departure between the center and edge strain-voltage curves at the NDR onset is consistent with the dissipated power being focused in the device center because of the resistance increase due to the approaching MIT. By considering the strain inhomogeneity defined as  $(\epsilon_{\text{center}} - \epsilon_{\text{edge}})/\epsilon_{\text{edge}}$  (Fig. 2F), we observe that this inhomogeneity, emerging at the NDR onset, fully develops, reaching  $\sim 40\%$ , at the voltage corresponding to the kink in the  $I$ - $V$  curve where the spatially uniform metallic state is expected to switch into a phase-separated state (high-resistance barrier splitting the metallic matrix) (35). Overall, the good correspondence between the strain development and  $I$ - $V$  curve features shows that electrically induced lattice expansion can be attributed to the applied voltage and dissipated power being focused within the high-resistance barrier when the device undergoes electrothermal MIT switching.

While the local temperature increase caused by Joule heating focusing can account for the general trend in the voltage-induced LSMO lattice expansion, several experimental observations highlight the important differences between the electrothermal effects and temperature-dependent lattice evolution at zero voltage. Electrothermal modeling predicts that the local LSMO temperature reaches a maximum at the barrier formation voltage threshold (35). Above this threshold, the barrier size grows as the applied voltage increases, but the barrier temperature stays constant. This limiting of the barrier temperature is due to the weak resistance-temperature dependence of LSMO in the high-temperature phase, which imposes a limit on the dissipated power focusing. The microdiffraction measurements, however, revealed that the lattice at the device

center (i.e., in the barrier region) keeps expanding as the applied voltage increases (Fig. 2E). This observed persistent strain increase suggests that local temperature is not the only parameter affecting the lattice constant. It is possible that when the local temperature increases, the associated local expansion can be partially hindered by the adjacent colder regions in the LSMO film and STO substrate enacting mechanical clamping. As the film remains continuous [no visible cracks or mechanical degradation appear in the devices even after millions of switching cycles (35)], the clamping can lead to strain accommodation, which often occurs by spatial modulations in the lattice parameter and/or twinning (44–46).

Closer examination of the diffraction peaks provides evidence of twin formation in the LSMO devices when the applied voltage is above the MIT triggering threshold. Fig. 3 shows 2D detector snapshots at the X-ray energies corresponding to the LSMO  $(007)_{\text{pc}}$  Bragg peak. At zero voltage (Fig. 3A), we observed a single diffraction peak, indicating structural homogeneity of the film in equilibrium. At 16 V (Fig. 3B), the peak splits into two well-defined peaks, which suggests that the film breaks into multiple structural domains of slightly different inclinations. The almost even splitting of the diffracted intensity between the two peaks implies that the twin domain size is much smaller compared to the  $\sim 5$   $\mu\text{m}$  spatial resolution in our microdiffraction experiments. At the twin domain boundaries, the lattice can be highly distorted, which may explain the observed Bragg peak broadening (Fig. 2C) and decreased diffraction intensity (Fig. 2B) when the applied voltage drives LSMO across the phase transition.

**Dark-Field X-ray Microscopy.** To further investigate lattice twinning in the switching devices, we employed DFXM, a technique that provides high-resolution, real-space imaging of the diffraction patterns originating from the different crystalline regions in a material (47, 48). The measurements were performed at the beamline 6-ID-C of the Advanced Photon Source at Argonne National Laboratory. Fig. 4A shows the schematics of the DFXM setup. The device area was illuminated by a parallel X-ray beam with an energy of 20 keV and at an incident angle of  $\sim 9.2^\circ$ , which corresponds to the  $(002)_{\text{pc}}$  LSMO Bragg peak. Imaging was achieved by passing the diffracted beam through a high-efficiency polymeric compound refractive lenses (pCRL) (47, 49). Similar to the lens in an optical microscope, the pCRL refracts the X-ray beam producing a magnified full-field view of the device on the scintillating X-ray detector. The pCRL had a focal length of

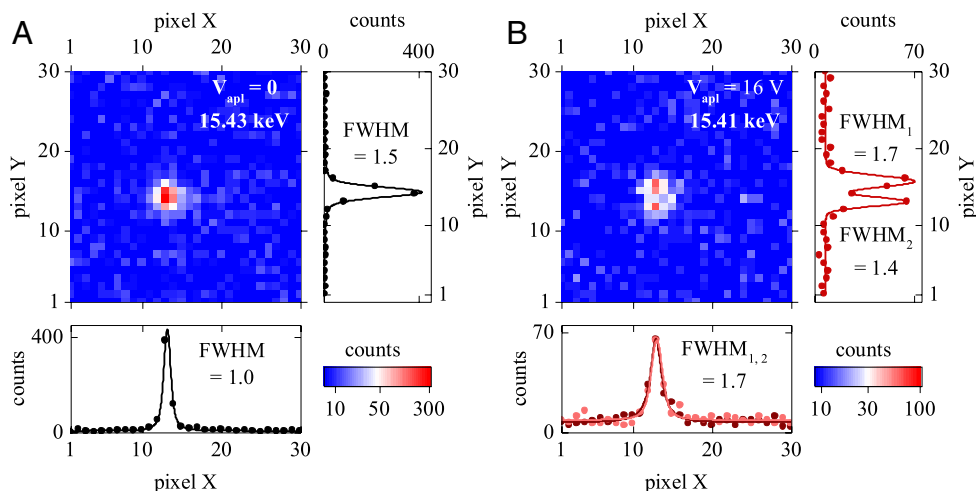


**Fig. 3.** 2D detector images of the LSMO  $(007)_{\text{pc}}$  Bragg peak acquired in equilibrium (0 V, panel A) and above the MIT triggering threshold (16 V, panel B). In equilibrium, there is a single diffraction peak indicating structural homogeneity of the LSMO thin film device. Above the MIT triggering threshold, the Bragg peak splits into two well-defined peaks, suggesting that the film breaks into structural twins with different orientations.

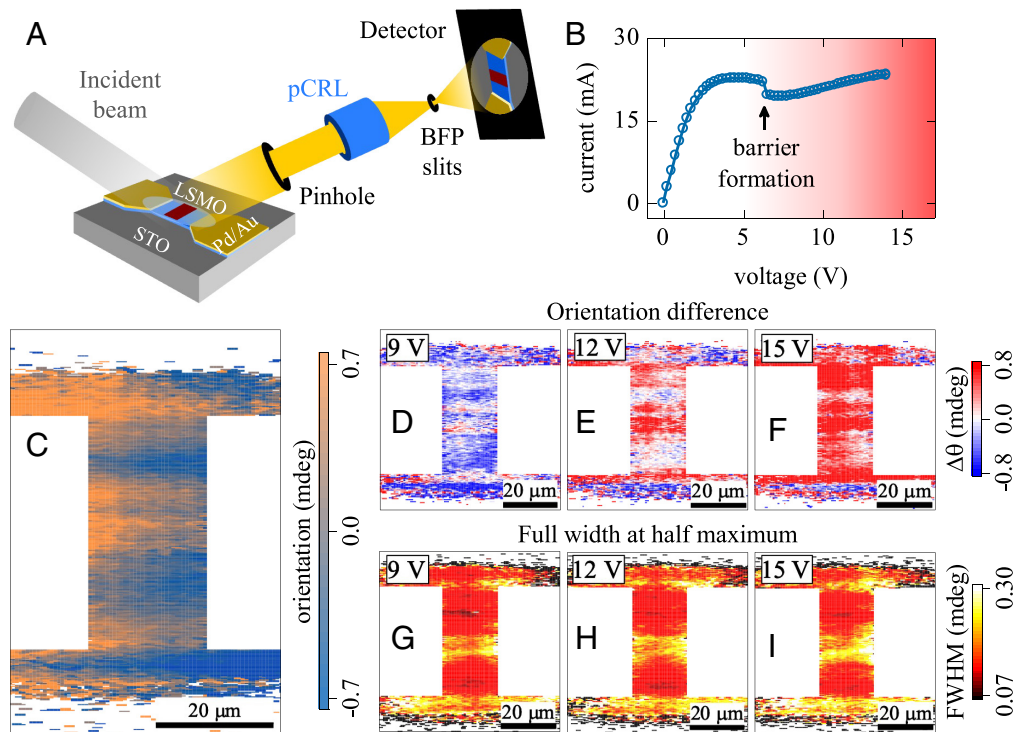


**Fig. 4.** (A) Schematic of the DFXM measurement setup. A parallel X-ray beam illuminates the entire device. The diffracted beam passes through a pCRL that refracts the beam producing a magnified device image on the detector. (B)  $I$ - $V$  curve of a  $20 \times 40 \mu\text{m}^2$  LSMO device at 115 K. (C) DFXM rocking curve COM map showing the lattice orientation distribution in the device at 0 V. (D–F) DFXM rocking curve COM difference maps corresponding to the applied voltages of 9 V (D), 12 V (E), and 15 V (F). These maps show how the lattice orientation changes during MIT triggering. (G–I) DFXM rocking curve width maps measured under applied voltages of 9 V (G), 12 V (H), and 15 V (I). These maps show how the rocking curve width changes throughout the device during MIT triggering. In the (D–I) maps, the formation of a barrier feature in the device center can be observed.

131 mm and was placed 140 mm from the sample. The detector was at a distance of 2.3 m from the pCRL. This geometry yielded an X-ray magnification factor of  $16\times$ . A  $50 \mu\text{m}$  pinhole and a set of slits in the back focal plane were used to improve the  $Q$ -space selectivity. An additional optical  $5\times$  magnification between the X-ray scintillating detector and optical camera (not shown in Fig. 4A) resulted in an overall  $80\times$  magnification. The imaging of the MIT switching in the LSMO device was performed at 115 K to avoid the presence of additional structural features due to the structural phase transition in the STO substrate at 105 K (50). The LSMO device size was  $20 \times 40 \mu\text{m}^2$ , which allowed the entire device area to be illuminated by the X-ray beam without the need to raster. Therefore, our DFXM setup was able to produce a full-field device image in a single exposure, unlike the microdiffraction approach in which the device area was scanned using the focused X-ray beam.

DFXM enabled imaging of small changes in the diffraction conditions when the applied voltage triggered the MIT in LSMO. The  $I$ - $V$  curve acquired during the X-ray measurements shows a clear discontinuity at 6.5 V (Fig. 4B), which can be attributed to the high-resistance barrier formation (35). The slightly different threshold voltage compared to the device studied in the microdiffraction experiments is due to the lower base temperature and different device dimensions in the DFXM measurements. The general electrical switching behavior in the two experiments, however, was identical: both  $I$ - $V$  curves in Figs. 2D and 4B display the onset of NDR and a discontinuous kink at the threshold voltage. Fig. 4C shows the measured real-space map of the lattice orientation distribution in the LSMO device at 0 V, i.e., in equilibrium. This map is based on recording a rocking curve around the  $(002)_{\text{pc}}$  Bragg peak of LSMO and plotting the center of mass (COM)

angle for each pixel. It can be observed that there are lattice orientation deviations, approximately  $\pm 0.5$  mdeg, throughout the device, which could be due to defects formed during the film growth and device fabrication or introduced by the repeated voltage cycling. To highlight the lattice orientation changes induced by the MIT switching, we subtracted this equilibrium orientation distribution map from the maps measured under applied voltages. Thus, Fig. 4D–F presents the differential maps of the lattice reorientation with respect to the initial state at 9 V, 12 V, and 15 V, i.e., voltages above the switching threshold.

We observed a significant crystal lattice reorientation throughout the entire device when LSMO undergoes the MIT switching. The spatial distribution of this reorientation is consistent with the voltage-induced high-resistance barrier formation. At 9 V (Fig. 4D), the area in the center of the device, which can be identified as the barrier, tilts toward higher angles (red color), while the crystal lattice in the rest of the device, constituting the metallic matrix, tilts toward opposite low angles (blue color), i.e., both switched and unswitched regions experience lattice tilting. This electrically induced lattice tilting in the high- and low-resistance regions reaches approximately  $\pm 0.8$  mdeg. As the voltage is increased to 12 V (Fig. 4E), the area occupied by the positive-angle-tilt region grows, which can be attributed to the barrier expansion. At 15 V (Fig. 4F), the positive-angle-tilt regions become prevalent throughout the device and only small, isolated pockets of the negative angle tilt regions remain. Importantly, positive- and negative-angle-tilt microscopic regions can be observed throughout the device, both in the switched barrier and unswitched metallic areas, at all explored applied voltages above the MIT triggering threshold. Therefore, DFXM imaging reveals that the entire device develops a complex structural modulation during the MIT switching.

The maps of the full width at half maximum (FWHM) of the rocking curves (Fig. 4 *G–I*) provide another perspective on the structural changes in LSMO induced by MIT triggering. We observed broadening of the rocking curves, indicating the increasing spread of the lattice orientation distribution as the device undergoes the switching. The rocking curve broadening appears to be spatially modulated. Larger broadening, up to  $\sim 0.3$  mdeg, occurs in the device center, which can be attributed to the voltage-induced high-resistance barrier formation. The FWHM of the rocking curves in the unswitched, metallic regions near the device edges remains at  $\sim 0.15$  mdeg. As the applied voltage increases, the center region with the increased FWHM expands, but it does not spread throughout the full device area even at 15 V, unlike in the maps of the lattice orientation distribution discussed in the previous paragraph (Fig. 4 *D–F*). We can conclude therefore, that similar to the microdiffraction measurements, DFXM shows the development of the lattice distortions across the device as the high-resistance barrier forms during the MIT switching, but the boundaries of the barrier region are not well defined from the structural perspective.

It is interesting to note that there is a spatial correlation between the equilibrium zero-voltage lattice orientation distribution (Fig. 4*C*) and structural changes induced by applying voltage (Fig. 4 *D–I*). It is likely that subtle defects present in the LSMO film may act as nucleation spots for the high-resistance barrier formation during MIT triggering. In an ideal, defect-free switching device, the barrier should form exactly at the device center (35). Unavoidable defects in a real sample may break the symmetry by locally increasing resistance. Locally increased resistance causes dissipated power focusing when the applied voltage is ramped up and, therefore, the high-resistance regions will undergo the MIT before the rest of the film. While the formation of defect regions in our LSMO samples was unintentional, a recent study has demonstrated that location and spatial path of the MIT switching can be predefined via defect engineering using focused ion beam irradiation (51).

## Discussion

Previous magneto-optical phase mapping measurements have shown a sharp contrast between the high-resistance barrier and metal matrix when an applied voltage triggers the phase transition in LSMO devices (35). Such clear spatial separation of metal/barrier phase regions is the direct consequence of magneto-optical imaging contrast sensitivity: The material can locally be either in the ferromagnetic metal or paramagnetic phase. The local X-ray diffraction measurements presented in this work (microdiffraction and DFXM) revealed that the boundary between the electrically induced high/low-resistance phase separation in LSMO is not structurally well defined. When an insulating barrier focuses Joule heating and causes local lattice thermal expansion, this expansion propagates partially throughout the entire device (Fig. 2*A*). Mechanical coupling between the hot high-resistance and cold metallic regions is likely the origin of lattice twinning, i.e., the formation of structural domains of different inclinations, which was evidenced by the i) reduced diffraction intensity (Fig. 2*B*), ii) increased Bragg peak width (Fig. 2*C*), iii) Bragg peak splitting (Fig. 3), and iv) orientation and width changes of the rocking curves (Fig. 4). The observation of these lattice deformations indicates that considering the switching spatial pattern simply as a metal/barrier/metal phase separation, as observed in the previous magneto-optical experiments (35), is incomplete. Based on magneto-optical measurements, it can be presumed that the barrier induced by MIT triggering is spatially uniform, i.e., applying

voltage brings LSMO in the same state as increasing temperature. X-ray microscopy, however, revealed that the crystal lattice in the electrically induced barrier region is twinned, which does not occur when warming up LSMO film past  $T_c$  at zero voltage (*SI Appendix*, Fig. S1). Magneto-optical measurements showed that device regions outside the high-resistance barrier remain in the ferromagnetic metal state, presumably unaffected by local MIT triggering in the barrier region. X-ray microscopy showed that metallic regions develop strain and experience lattice tilting, which does not occur in thermal equilibrium at zero voltage (*SI Appendix*, Fig. S1). Because such lattice deformations are not present during equilibrium thermal expansion, it is not justified to directly compare the voltage-induced lattice expansion and equilibrium thermal expansion, for example, to estimate the local temperature increase during the MIT switching, i.e., to use strain as a temperature probe.

Lattice twinning during the MIT switching in LSMO (Fig. 4 *D–F*) bears a strong resemblance to the well-established phase separation phenomenon in many members of the rare-earth manganite family (52). Stable coexistence over a broad temperature range of ferromagnetic metal and charge-ordered insulator domains of nano- to microscale sizes has been observed in materials such as (La,Ca)MnO<sub>3</sub> (53), (La,Pr,Ca)MnO<sub>3</sub> (54), and (Nd,Sr)MnO<sub>3</sub> (55). Optimally doped LSMO with the La:Sr ratio of 0.7:0.3 studied in this work does not exhibit phase separation in equilibrium, however, phase separation in LSMO can emerge when the La:Sr ratio deviates from the optimal doping (56). Our structural microscopy does not directly show whether the different lattice twins in the switching devices have different electronic/magnetic properties, as in the case of canonical phase separation. Based on the natural proclivity of rare-earth manganites to exhibit phase separation and their extreme sensitivity to structural imperfections, we hypothesize a possibility that applying voltage may drive LSMO both along the temperature axis (i.e., Joule heating) and doping axis of the phase diagram bringing the material into the state where a structural/electronic/magnetic phase separation may emerge. Additional experiments are needed to test this hypothesis.

Joule heating in LSMO devices also causes thermal expansion in the underlying STO substrate (gray symbols in Fig. 2*E*). The substrate expansion, however, is a factor of  $\sim 3$  to 5 smaller (depending on the position) compared to the film, which suggests that the *c/a* ratio in LSMO could be changing when the applied voltage is ramped up. It is well established that the lattice strain and *c/a* ratio have a major contribution in determining electrical and magnetic properties in complex oxide thin films (57, 58). Specifically in LSMO, strain can change the phase transition temperature (59), magnetic anisotropy (60–62), magnetotransport (63), magnetization domain configuration (64), etc. The voltage-induced inhomogeneous lattice expansion occurring throughout the entire LSMO device, as observed in this work, can play an important role in the process of electrical MIT triggering as well as contribute to the previously reported magnetic anisotropy change and anomalous magnetotransport properties in LSMO switching devices (36, 37). Overall, our X-ray microscopy studies showed that electrical MIT triggering is a complex process that produces local structural states that differ qualitatively from the equilibrium, zero-voltage thermal evolution of the crystal lattice.

## Conclusions

Local structural studies revealed that electrical MIT triggering is accompanied by the development of substantial inhomogeneous lattice strain. The material under study, LSMO, does not

undergo a 1st-order structural transition coinciding with the MIT, therefore, the observed structural inhomogeneities cannot be attributed to the crystal symmetry mismatch between the low- and high-temperature phases. Because of this absence of material-specific symmetry considerations, the emergence of complex structural patterns may be a general feature of electrical MIT switching. The measured voltage-induced strain exhibited a nonuniform profile across the device length, i.e., larger strain develops in the device center than at the edges. This strain non-uniformity is consistent with Joule heating being focused in the regions where LSMO locally undergoes switching into the high-resistance phase, resulting in a higher local temperature and, consequently, in a larger thermal expansion. While the Joule-heating-driven lattice expansion is anticipated, local diffraction measurements further revealed unexpected qualitative differences between the electrothermal and temperature-dependent crystal structure evolution under equilibrium conditions. We observed lattice tilting, twinning, and development of pronounced lattice distortions during MIT triggering. These voltage-induced structural changes are not confined only within the local region where the MIT is triggered. The lattice distortions propagate throughout the device, indicating the nonlocal nature of electrical MIT triggering. Microdiffraction experiments showed that the lattice expansion within the entire device area persistently increases as the voltage is being ramped up past the MIT triggering threshold, even though a constant temperature differential between the unswitched metal regions and switched barrier region is expected to establish after the barrier forms inside the metallic matrix. This persistent lattice expansion suggests that local temperature is not the only factor that determines the voltage-induced structural evolution. DFXM imaging showed that the crystal lattice experiences tilting and orientation distribution spread in the switched and unswitched regions, indicating that both regions in the switching device are structurally nonuniform. Development of these structural inhomogeneities revealed by the X-ray microscopy highlights the complexity of electrical MIT triggering that is not captured in conventional phase mapping experiments. Because lattice inhomogeneities do not emerge when increasing temperature at zero voltage, our experiments indicate that electrical MIT switching brings the material in a qualitatively distinct structural state as compared to thermal equilibrium. It is well known that MIT materials are extremely sensitive to even minute crystal structure imperfections. Our observations of the inhomogeneous strain development during MIT triggering suggest that electrically induced structural changes may play a significant role in the switching process, for example, influencing properties such as switching threshold voltage/current or the shape and size of the switched region. Multiple recent experimental efforts have been dedicated to decoupling electronic and structural transitions in the MIT materials (65–67), which is partially motivated by improving the switching energy

efficiency. The X-ray microscopy experiments showed that a strong crystal lattice response still occurs during the electrically induced MIT even when the MIT does not coincide with a structural phase transition, which must entail an associated energy cost. On the other hand, local voltage-induced inhomogeneous strain and lattice distortions may drive the material into a structural configuration that differs from the thermal equilibrium state, providing an unconventional way to explore basic nonequilibrium phenomena in MIT systems and opening opportunities for the functional device design.

## Materials and Methods

**Film Growth.** LSMO films were grown on a (001)-oriented STO substrate using pulsed laser deposition with a laser fluence of 0.6 J/cm<sup>2</sup> and a frequency of 1 Hz. During the growth, the substrate temperature was held at 700 °C with an oxygen pressure of 0.3 Torr. Postdeposition, the film was slowly cooled to room temperature in 300 Torr O<sub>2</sub> to ensure proper oxygen stoichiometry.

**Device Fabrication.** Two-terminal devices were fabricated using a three-step procedure. First, optical lithography and metal lift-off were used to prepare (20 nm Pd)/(20 nm Au) electrodes. These electrodes provided low-resistance contacts for the LSMO devices. Second, optical lithography and Ar ion milling were used to define isolated LSMO devices. Third, optical lithography and metal lift-off were used to prepare (20 nm Ti)/(120 nm Au) electrodes. These electrodes provided strong surface adhesion and were used for wire bonding. All metal electrodes were deposited using standard e-beam evaporation. Postfabrication, the samples were annealed in O<sub>2</sub> atmosphere to eliminate surface conductivity of the STO substrate induced by the Ar milling.

**Characterization.** *I*-*V* curves were acquired using a Keithley 2450 source meter. Temperature-dependent X-ray measurements (SI Appendix, Fig. S1) were performed in a lab-based X-ray diffractometer Rigaku SmartLab using unpatterned LSMO films. Details of the microdiffraction and DFXM measurements are provided in the manuscript text.

**Data, Materials, and Software Availability.** All study data are included in the article and/or SI Appendix.

**ACKNOWLEDGMENTS.** This work was supported as part of the “Quantum Materials for Energy Efficient Neuromorphic Computing” (Q-MEEN-C), an Energy Frontier Research Center funded by the U.S. Department of Energy, Office of Science, Basic Energy Sciences under Award No. DESC0019273. This research used resources of the Advanced Light Source, a U.S. Department of Energy (DOE) Office of Science User Facility under contract no. DE-AC02-05CH11231. This research used resources of the Advanced Photon Source, a U.S. DOE Office of Science user facility operated for the DOE Office of Science by Argonne National Laboratory under Contract No. DE-AC02-06CH11357. We would like to thank the Karlsruhe Nano Micro Facility for the fabrication of the polymer X-ray optics.

Author affiliations: <sup>a</sup>Department of Physics and Astronomy, University of Denver, Denver, CO 80210; <sup>b</sup>Department of Physics, University of California San Diego, La Jolla, CA 92093; <sup>c</sup>X-ray Science Division, Argonne National Laboratory, Argonne, IL 60439; <sup>d</sup>Department of Materials Science and Engineering, University of California Davis, Davis, CA 95616; and <sup>e</sup>Advanced Light Source, Lawrence Berkeley National Laboratory, Berkeley, CA 94720

1. Y. Zhou, S. Ramanathan, Mott memory and neuromorphic devices. *Proc. IEEE* **103**, 1289 (2015).
2. J. del Valle, J. G. Ramirez, M. J. Rozenberg, I. K. Schuller, Challenges in materials and devices for resistive-switching-based neuromorphic computing. *J. Appl. Phys.* **124**, 211101 (2018).
3. M. Son *et al.*, Excellent selector characteristics of nanoscale VO<sub>2</sub> for high-density bipolar ReRAM applications. *IEEE Electron Device Lett.* **32**, 1579 (2011).
4. J. Park *et al.*, Multi-layered NiO<sub>x</sub>/NbO<sub>x</sub>/NiO<sub>x</sub> fast drift-free threshold switch with high Ion/loff ratio for selector application. *Sci. Rep.* **7**, 4068 (2017).
5. M. Liu *et al.*, Terahertz-field-induced insulator-to-metal transition in vanadium dioxide metamaterial. *Nature* **487**, 345 (2012).
6. N. A. Butakov *et al.*, Broadband electrically tunable dielectric resonators using metal-insulator transitions. *ACS Photonics* **5**, 4056 (2018).
7. S. Yang, M. Vaseem, A. Shamim, Fully inkjet-printed VO<sub>2</sub>-based radio-frequency switches for flexible reconfigurable components. *Adv. Mater. Technol.* **4**, 1800276 (2019).
8. M. D. Pickett, G. Medeiros-Ribeiro, R. S. Williams, A scalable neuristor built with mott memristors. *Nat. Mater.* **12**, 114 (2013).
9. W. Yi *et al.*, Biological plausibility and stochasticity in scalable VO<sub>2</sub> active memristor neurons. *Nat. Commun.* **9**, 4661 (2018).
10. J. del Valle, P. Salev, Y. Kalchheim, I. K. Schuller, A caloritronics-based mott neuristor. *Sci. Rep.* **10**, 4292 (2020).
11. J. Del Valle *et al.*, Generation of tunable stochastic sequences using the insulator-metal transition. *Nano Lett.* **22**, 1251 (2022).
12. E. Qiu *et al.*, Stochasticity in the synchronization of strongly coupled spiking oscillators. *Appl. Phys. Lett.* **122**, 094105 (2023).
13. E. Qiu *et al.*, Stochastic transition in synchronized spiking nanooscillators. *Proc. Natl. Acad. Sci. U.S.A.* **120**, e2303765120 (2023).
14. J. S. Brockman *et al.*, Subnanosecond incubation times for electric-field-induced metallization of a correlated electron oxide. *Nat. Nanotechnol.* **9**, 453 (2014).



15. Y. Kalcheim *et al.*, Non-thermal resistive switching in mott insulator nanowires. *Nat. Commun.* **11**, 2985 (2020).
16. M. Medarde, P. Lacorre, K. Conder, F. Fauth, A. Furrer, Giant  $^{16}\text{O}$ - $^{18}\text{O}$  isotope effect on the metal-insulator transition of  $\text{RNiO}_3$  Perovskites (R=Rare Earth). *Phys. Rev. Lett.* **80**, 2397 (1998).
17. I. Vobornik *et al.*, Electronic-structure evolution through the metal-insulator transition in  $\text{RNiO}_3$ . *Phys. Rev. B* **60**, R8426 (1999).
18. M. W. Haverkort *et al.*, Orbital-assisted metal-insulator transition in  $\text{VO}_2$ . *Phys. Rev. Lett.* **95**, 196404 (2005).
19. B. Zwartsenberg *et al.*, Spin-orbit-controlled metal-insulator transition in  $\text{Sr}_2\text{IrO}_4$ . *Nat. Phys.* **16**, 290 (2020).
20. J. Trastoy *et al.*, Magnetic field frustration of the metal-insulator transition in  $\text{V}_2\text{O}_3$ . *Phys. Rev. B* **101**, 245109 (2020).
21. Y. Feng *et al.*, A continuous metal-insulator transition driven by spin correlations. *Nat. Commun.* **12**, 2779 (2021).
22. Y. Kalcheim *et al.*, Robust coupling between structural and electronic transitions in a mott material. *Phys. Rev. Lett.* **122**, 057601 (2019).
23. S. Cheng *et al.*, Inherent stochasticity during insulator-metal transition in  $\text{VO}_2$ . *Proc. Natl. Acad. Sci. U.S.A.* **118**, e2105895118 (2021).
24. B. Simon Mun *et al.*, Role of joule heating effect and bulk-surface phases in voltage-driven metal-insulator transition in  $\text{VO}_2$  crystal. *Appl. Phys. Lett.* **103**, 061902 (2013).
25. A. G. Shabalin *et al.*, Nanoscale imaging and control of volatile and non-volatile resistive switching in  $\text{VO}_2$ . *Small* **16**, 2005439 (2020).
26. P. G. Radaelli *et al.*, Structural effects on the magnetic and transport properties of Perovskite  $\text{A}_{1-x}\text{A}'_x\text{MnO}_3$  ( $x=0.25, 0.30$ ). *Phys. Rev. B* **56**, 8265 (1997).
27. J. Alonso, M. Martínez-Lope, M. Casais, J. García-Muñoz, Room-temperature monoclinic distortion due to charge disproportionation in  $\text{RNiO}_3$  perovskites with small rare-earth cations (R=Ho, Y, Er, Tm, Yb, and Lu): A neutron diffraction study. *Phys. Rev. B* **61**, 1756 (2000).
28. S. Kumar *et al.*, Physical origins of current and temperature controlled negative differential resistances in  $\text{NbO}_2$ . *Nat. Commun.* **8**, 658 (2017).
29. C. Adda *et al.*, Direct observation of the electrically triggered insulator-metal transition in  $\text{V}_3\text{O}_5$  far below the transition temperature. *Phys. Rev. X* **12**, 011025 (2022).
30. J. del Valle *et al.*, Dynamics of the electrically induced insulator-to-metal transition in rare-earth nickelates. *Phys. Rev. B* **104**, 165141 (2021).
31. Y. Ogimoto *et al.*, Strain-induced crossover of the metal-insulator transition in perovskite manganites. *Phys. Rev. B* **71**, 060403 (2005).
32. J. Liu *et al.*, Strain-mediated metal-insulator transition in epitaxial ultrathin films of  $\text{NdNiO}_3$ . *Appl. Phys. Lett.* **96**, 233110 (2010).
33. Y. Kalcheim *et al.*, Structural manipulation of phase transitions by self-induced strain in geometrically confined thin films. *Adv. Funct. Mater.* **30**, 2005939 (2020).
34. E. Barazani *et al.*, Positive and negative pressure regimes in anisotropically strained  $\text{V}_2\text{O}_3$  films. *Adv. Funct. Mater.* **33**, 2211801 (2023).
35. P. Salev *et al.*, Transverse barrier formation by electrical triggering of a metal-to-insulator transition. *Nat. Commun.* **12**, 5499 (2021).
36. P. Salev *et al.*, Voltage-controlled magnetic anisotropy enabled by resistive switching. *Phys. Rev. B* **107**, 054415 (2023).
37. P. Salev *et al.*, Magnetoresistance anomaly during the electrical triggering of a metal-insulator transition. *Phys. Rev. B* **108**, 174434 (2023).
38. R. V. Chopdekar *et al.*, Nanostructured complex oxides as a route towards thermal behavior in artificial spin ice systems. *Phys. Rev. Mater.* **1**, 24401 (2017).
39. D. Y. Sasaki *et al.*, Formation of complex spin textures in thermally demagnetized  $\text{La}_0.7\text{Sr}_{0.3}\text{MnO}_3$  artificial-spin-ice structures. *Phys. Rev. Appl.* **17**, 64057 (2022).
40. Y. Tokura, Critical features of colossal magnetoresistive manganites. *Rep. Prog. Phys.* **69**, 797 (2006).
41. J. del Valle *et al.*, Spatiotemporal characterization of the field-induced insulator-to-metal transition. *Science* **373**, 907 (2021).
42. M. Lange *et al.*, Imaging of electrothermal filament formation in a mott insulator. *Phys. Rev. Appl.* **16**, 054027 (2021).
43. T. Luibrand *et al.*, Characteristic length scales of the electrically induced insulator-to-metal transition. *Phys. Rev. Res.* **5**, 013108 (2023).
44. J.-L. Maurice *et al.*, Strain relaxation in the epitaxy of  $\text{La}_{2/3}\text{Sr}_{1/3}\text{MnO}_3$  grown by pulsed-laser deposition on  $\text{SrTiO}_3(001)$ . *Philos. Mag.* **83**, 3201 (2003).
45. M.-W. Chu, I. Szafraniak, D. Hesse, M. Alexe, U. Gösele, Elastic coupling between  $90^\circ$  twin walls and interfacial dislocations in epitaxial ferroelectric perovskites: A quantitative high-resolution transmission electron microscopy study. *Phys. Rev. B* **72**, 174112 (2005).
46. A. Vailionis *et al.*, Misfit strain accommodation in epitaxial  $\text{ABO}_3$  perovskites: Lattice rotations and lattice modulations. *Phys. Rev. B* **83**, 64101 (2011).
47. Z. Qiao *et al.*, A large field-of-view high-resolution hard x-Ray microscope using polymer optics. *Rev. Sci. Instrum.* **91**, 113703 (2020).
48. J. Plumb *et al.*, Dark field X-Ray microscopy below liquid-helium temperature: The case of  $\text{NaMnO}_2$ . *Mater. Charact.* **204**, 113174 (2023).
49. F. Marschall *et al.*, X-Ray full field microscopy at 30 KeV. *J. Phys. Conf. Ser.* **499**, 012007 (2014).
50. R. A. Cowley, The phase transition of strontium titanate. *Philos. Trans. R. Soc. London Series A: Math. Phys. Eng. Sci.* **354**, 2799 (1996).
51. N. Ghazikhanian *et al.*, Resistive switching localization by selective focused ion beam irradiation. *Appl. Phys. Lett.* **123**, 123505 (2023).
52. E. Dagotto, T. Hotta, A. Moreo, Colossal magnetoresistant materials: The key role of phase separation. *Phys. Rep.* **344**, 1 (2001).
53. J. Tao *et al.*, Direct imaging of nanoscale phase separation in  $\text{La}_{0.55}\text{Ca}_{0.45}\text{MnO}_3$ : Relationship to colossal magnetoresistance. *Phys. Rev. Lett.* **103**, 097202 (2009).
54. T. Miao *et al.*, Direct experimental evidence of physical origin of electronic phase separation in manganites. *Proc. Natl. Acad. Sci. U.S.A.* **117**, 7090 (2020).
55. K. Lai *et al.*, Mesoscopic percolating resistance network in a strained manganite thin film. *Science* **329**, 190 (2010).
56. R.-W. Li *et al.*, Direct observation of phase separation in  $\text{La}_{0.45}\text{Sr}_{0.55}\text{MnO}_{3-\delta}$ . *J. Appl. Phys.* **92**, 7404 (2002).
57. D. G. Schlom *et al.*, Elastic strain engineering of ferroic oxides. *MRS Bull.* **39**, 118 (2014).
58. S. Dhole, A. Chen, W. Nie, B. Park, Q. Jia, Strain engineering: A pathway for tunable functionalities of perovskite metal oxide films. *Nanomaterials* **12**, 835 (2022).
59. P. Dey, T. K. Nath, A. Taraphder, Effect of substrate-induced strain on transport and magnetic properties of epitaxial  $\text{La}_{0.66}\text{Sr}_{0.33}\text{MnO}_3$  thin films. *Appl. Phys. Lett.* **91**, 012511 (2007).
60. Y. Suzuki, H. Y. Hwang, S.-W. Cheong, R. B. van Dover, The role of strain in magnetic anisotropy of manganite thin films. *Appl. Phys. Lett.* **71**, 140 (1997).
61. L. M. Berndt, V. Balbarin, Y. Suzuki, Magnetic anisotropy and strain states of (001) and (110) colossal magnetoresistance thin films. *Appl. Phys. Lett.* **77**, 2903 (2000).
62. P. Perna *et al.*, Tailoring magnetic anisotropy in epitaxial half metallic  $\text{La}_{0.7}\text{Sr}_{0.3}\text{MnO}_3$  thin films. *J. Appl. Phys.* **110**, 013919 (2011).
63. F. Yang *et al.*, Strain engineering to control the magnetic and magnetotransport properties of  $\text{La}_{0.67}\text{Sr}_{0.33}\text{MnO}_3$  thin films. *Appl. Phys. Lett.* **97**, 092503 (2010).
64. J. Dho, Y. N. Kim, Y. S. Hwang, J. C. Kim, N. H. Hur, Strain-induced magnetic stripe domains in  $\text{La}_{0.7}\text{Sr}_{0.3}\text{MnO}_3$  thin films. *Appl. Phys. Lett.* **82**, 1434 (2003).
65. Z. Tao *et al.*, Decoupling of structural and electronic phase transitions in  $\text{VO}_2$ . *Phys. Rev. Lett.* **109**, 166406 (2012).
66. A. S. McLeod *et al.*, Nanotextured phase coexistence in the correlated insulator  $\text{V}_2\text{O}_3$ . *Nat. Phys.* **13**, 80 (2017).
67. J. Xu, D. Chen, S. Meng, Decoupled ultrafast electronic and structural phase transitions in photoexcited monoclinic  $\text{VO}_2$ . *Sci. Adv.* **8**, eadd2392 (2022).